Enhancement of Evaporation from a Large Northern Lake by the Entrainment of Warm, Dry Air

PETER D. BLANKEN

Department of Geography and Program in Environmental Studies, University of Colorado, Boulder, Colorado

WAYNE R. ROUSE

School of Geography and Geology, McMaster University, Hamilton, Ontario, Canada

WILLIAM M. SCHERTZER

National Water Research Institute, Burlington, Ontario, Canada

(Manuscript received 26 September 2002, in final form 14 March 2003)

ABSTRACT

The turbulent exchange of water vapor and heat were measured above Great Slave Lake, Northwest Territories, Canada, using the eddy covariance method for most of the ice-free period in 1997, 1998, and 1999. In all years, evaporation tended to occur in episodic pulses, lasting 52–78 h, between which quiescent periods dominated. The contributions of these evaporation pulses to the measured total evaporation were 45%, 65%, and 47% for 1997, 1998, and 1999, respectively, yet occurred on only 24% (1997), 37% (1998), and 25% (1999) of the total number of days observed. Despite the suppression of turbulent mixing, due to the stable atmospheric conditions that dominated much of the ice-free periods, analyses of high-frequency wind, air temperature, and humidity data revealed that evaporation was enhanced by the mixing of warm, dry air down to the lake surface. Conditional sampling of turbulent measurements showed that these sweeps of warm, dry air were infrequent, yet were the dominant turbulent transfer mechanism. Because the approximately 3-day-long evaporation pulses were composed of an aggregation of sweeps, measurements of air–lake turbulent heat exchange needed to be made at a high frequency in order to capture these significant events. Implications of climate variability on the mechanisms that control short- and long-term evaporation rates were discussed, in terms of the positive feedback that developed between entrainment and evaporation.

1. Introduction

Large lakes are capable of modifying the energy and water cycles of the land that surrounds them. For example, differences in the surface energy balance of water versus land leads to large differences in surface temperatures over each surface. When mid- and high-latitude lakes are ice free in the late fall and early winter, they help maintain higher air temperatures and promote overcast conditions in the surrounding area that would otherwise be much colder and drier. Lake-effect snow is common at these times, which can dramatically influence the local terrestrial water balance. Conversely, in the spring, a cold lake surface, relative to the surrounding terrain, can retard the terrestrial warming process. Large lakes can also help spawn, maintain, or enhance significant storms and high winds, which, in turn, can impact the surrounding terrain. These large-lake effects are perhaps exacerbated at high latitudes, where a sharp contrast between lake and land surface temperatures develop as the seasons change quickly.

In this and companion papers (e.g., Blanken et al. 2000; Rouse et al. 2003b; Schertzer et al. 2000; Schertzer et al. 2003); the various aspects of the surface energy balance of Great Slave Lake, Northwest Territories, Canada are described. The motivation is to understand the role that lakes play in the energy and water cycles of the Mackenzie River basin, under the umbrella of the Global Energy and Water Cycle Experiment (GEWEX) (see, Stewart et al. 1998; Rouse et al. 2003a). Measurements during most of the ice-free periods in 1997–99 are presented, including the Canadian Enhanced GEWEX Study (CAGES) that occurred in 1998.

Lakes are a ubiquitous part of the northern landscape, and within the Mackenzie drainage basin, several ''great lakes'' are found. In addition to Great Slave Lake, within the drainage basin are Great Bear Lake and Lake Athabasca. Globally, these lakes represent a significant vol-

Corresponding author address: Peter D. Blanken, Department of Geography and Program in Environmental Studies, University of Colorado, 260 UBC, Boulder, CO 80309-0260.
E-mail: blanken@colorado.edu

ume of freshwater, with Great Slave Lake (with a maximum depth of 614 m), which is ranked the deepest in North America, ranking sixth globally, and Great Bear Lake ranking 11th and 13th respectively, in terms of water volume, and 11th and 9th, respectively, in terms of surface area. Within the Mackenzie basin, these two lakes cover 3.3% of the area (59 896 km^2). A hypothesis is that findings on Great Slave Lake are entirely applicable to Great Bear Lake and other large lakes in the Mackenzie basin.

A previous study (Blanken et al. 2000) found that both the lake and atmosphere were thermally stable for much of the ice-free period. The lake was thermally stratified (baring occasional strong winds capable of mixing down to the thermocline depth of 15 m) between roughly mid-July and early September 1998, with a predominantly stable atmosphere. Despite the strong damping of convectively driven turbulence in this situation, evaporation was ''episodic'' with 50% of the total evaporation occurring over only 20% of the days in 1998. Those using the eddy covariance technique, based on high-frequency (e.g., 10 Hz) sampling, also find high evaporation rates even during atmospherically stable conditions (e.g., Heikinheimo et al. 1999), whereas those estimating evaporation from hourly mean buoy data do not (e.g., Laird and Kristovich 2002). It is reasonable to assume that the vertical mixing (entrainment) of warm, dry air from above the atmosphere's thermal capping inversion caused these episodic evaporation events. Such events could only be captured with high-frequency measurements, and could be significant in terms of increasing the lake's evaporative water loss, thus, affecting the regional water cycle. Others report evidence of entrainment across a marine boundary layer (Russell et al. 1998), even during stable conditions at night above a terrestrial surface (Sun et al. 2002).

Here, a detailed study on the nature of the enhancement of evaporation from Great Slave Lake by the entrainment of this warm, dry air is presented. Several signal-processing tools are employed to examine these events, including an analysis of high-frequency (10 Hz) turbulence, air temperature, and humidity data. The objectives are to quantify the mechanism, importance, and role of these events in the evaporation of water from a large northern lake.

2. Study site

Instruments were located on a small rock island located near the main body of the lake 12 km from shore (Inner Whaleback Islands; 61.92°N, 113.73°W), 70 km southeast of Yellowknife, Northwest Territories, Canada, and 150 km northeast of Hay River (Fig. 1). The site was carefully chosen to be in a location where the surrounding water depth was close to the mean lake depth of 50 m (excluding the eastern arm, where depths can exceed 600 m). The island's height above the mean water surface, width, and length are approximately 10, 100, and 180 m, respectively, with the long axis oriented roughly east–west. Calculation of the flux footprint (Schuepp et al. 1990), or upwind distance contributing to the turbulent flux measurements (fetch), indicated that 80% of turbulent flux measurements were sampled over an upwind distance extending 4.9, 5.9, and 8.4 km (daytime, neutral, and nighttime periods, respectively) from the site (Blanken et al. 2000). Using passive microwave satellite data, the main body of the lake was ice free on 20 June 1997, 1 June 1998, and 10 June 1999, and was ice covered by 13 December 1997, 8 January 1999, and 10 December 1999 (Walker et al. 1999). The exceptionally long ice-free season in 1998 was synchronous with above-average air temperatures and an abnormally strong El Niño (Blanken et al. 2000). Descriptions of the general characteristics of the lake can be found in Rawson (1950), of ice conditions in Walker et al. (1999), and of thermal structure and bathymetry in Schertzer et al. (2000).

3. Theory and methods

In turbulent flow, wind velocity components (vertical wind, w) and a scalar quantity transported by this wind (s) vary irregularly in space and time. Through what is known as Reynolds decomposition, instantaneous values of w and s can be decomposed into a mean (overbars) and fluctuating part (primes): $w = \overline{w} + w'$; $s = \overline{s} + s'$. The eddy covariance (or correlation) method calculates a flux from high-frequency (typically 10–20 Hz) measurements of w and s. Over an arbitrary time interval (1.0 h, in this case), deviations of w and s from the time-averaged means are calculated, and the flux is calculated from the covariance of w' and s' over the time interval. Using Reynolds decomposition, the flux of s is given as

$$\begin{aligned} \text{flux}(s) &= \overline{(\overline{w} + w')(\overline{s} + s')} \\ &= \overline{\overline{w}\,\overline{s}} + \overline{\overline{w}s'} + \overline{w'\overline{s}} + \overline{w's'}, \end{aligned} \tag{1}$$

where the second and third terms on the right-hand side of Eq. (1) should be zero because, by definition, the mean of any fluctuating variable is zero (i.e., $\overline{w'} = 0$, $\overline{s'} = 0$). The first term on the right-hand side of Eq. (1) should be approximately zero if updrafts are roughly balanced by downdrafts (i.e., the mean vertical velocity is approximately zero). Hence, the latent heat flux, λE (product of the latent heat of vaporization, λ, and the evaporation rate, E) and the sensible heat flux, H, were calculated as $\lambda E = \lambda \overline{w'\rho_v'}$ and $H = \rho_a c_p \overline{w'T'}$, where T is the air temperature, ρ_v is the vapor density, ρ_a is the air density, and c_p is the specific heat of dry air (a positive flux is directed away from the surface, negative flux is directed toward the surface). The momentum flux was calculated as $\tau = \rho_a \overline{w'u'}$, where u is the scalar horizontal wind speed and the friction velocity is $u^* = \sqrt{\tau/\rho_a}$. Therefore, the time-averaged turbulent fluxes are essentially aggregated from the high-frequency time se-

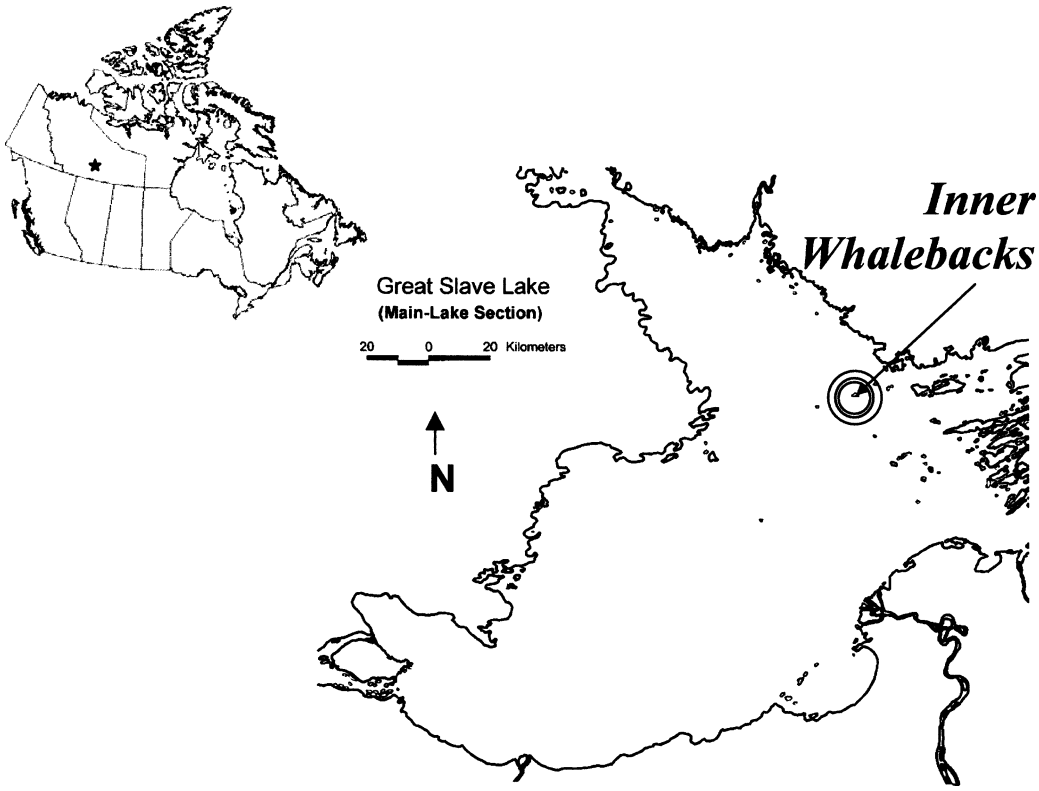

FIG. 1. Location of Great Slave Lake, Northwest Territories, Canada (insert), and the study site, at the Inner Whaleback Islands. Circles indicate a radii of 4.9, 5.9, and 8.4 km, corresponding to the distance where 80% of the turbulent fluxes were sampled during typical daytime, neutral, and nighttime atmospheric stability conditions, respectively.

ries. How these short-term events (seconds to minutes) are scaled up to long-term events (days to weeks) is described in this paper. It is unique to use the eddy covariance method to make long-term, direct measurements of λE and H over large bodies of water from the same location. Usually, λE is estimated using long-term (i.e., daily or even monthly) buoy data, and, as a result, the fast λE events (i.e., seconds and hours) that are described here as important are averaged out and simply not resolved. For example, Bates and Merlivat (2001) found that the air–sea carbon dioxide (CO_2) flux is up to 3 times greater if hourly rather than daily averaged wind data are used. The data and analysis presented here show the influence of short-term events on long-term observations of E.

A detailed description of the instrumentation is found in Blanken et al. (2000), so, here, some of the instruments and signal-processing analysis tools used to quantify the nature the vertical entrainment of warm, dry air, and its role in enhancing evaporation are described. Measurements of the vertical wind speed (w, m s^{-1}), scalar horizontal wind speed (u, m s^{-1}), air temperature (T, °C), and vapor density (ρ_v, g m^{-3}) were made at a frequency (f, Hz) of 20 Hz by the Mk2 Hydra eddy covariance system. The Hydra was supported by a telescopic pneumatic mast at a height (z) of 6.9 m above the ground surface, equal to ≈16.9 m above the mean water surface, away from the influence of spray from the lake. Vertical wind speed was measured with a pair of vertically oriented ultrasonic transducers separated by 200 mm, exchanging 40-kHz ultrasonic waves. A fast-response three-cup anemometer (starting threshold of less than 0.15 m s^{-1}), located above the ultrasonic transducers, measured u, and T was measured with a fast-response 38-μm-diameter chromel-copper thermocouple mounted horizontally and centered between the ultrasonic transducers. Vapor density was measured with an infrared hygrometer with a vertically oriented source and detector separated by 250 mm, located parallel and behind the ultrasonic transducers. A full description of the Mk2 Hydra is given by Shuttleworth et al. (1988).

The Hydra was used to measure the hourly λE and H for most of the ice-free period in 1997, 1998, and 1999, supplemented by the supporting measurements described below (see Figs. 2–9). To examine the role of short-term phenomena (occurring over time periods on the order of seconds; see Figs. 10–16) in the long-term daily and seasonal patterns of λE and H, the detailed high-frequency (i.e., 10 Hz) data were required. The Hydra, however, did not routinely retain the high-frequency data, due to a limited memory storage ca-

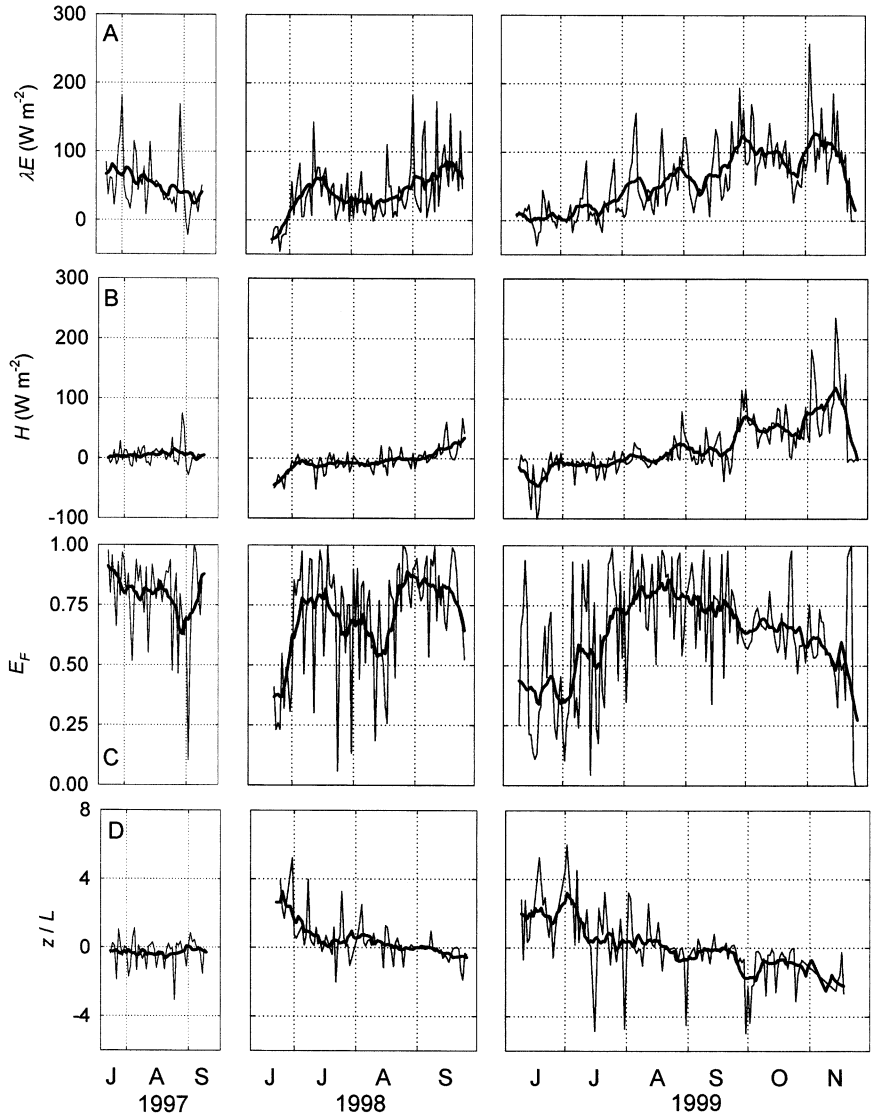

FIG. 2. Annual patterns of the latent heat flux (A, λE), sensible heat flux (B, H), evaporative fraction [C, $E_F = |\lambda E|/(|\lambda E| + |H|)$], and the observation height divided by the Monin–Obukhov length (D, z/L). The patterns of the 24-h (UTC) means (thin lines) are illustrated by 10-day running means (thick lines).

pacity. Therefore, the Hydra was temporarily modified to retain these data by connecting an external datalogger (Campbell Scientific, model 21X) in parallel to the Hydra. Voltages from each sensor were recorded at f = 10 Hz, $f/2$ of the Hydra, on 23 June 1998, over a 1.5-h period starting at 2010 UTC. During this cloud-free period, $\overline{u}$ was 5.2 m s^{-1} from the west, resulting in an estimated wave height of 1 m (Hudson 1991). Atmospheric stability, quantified by the ratio of z to the Monin–Obukhov length L was 0.17, indicating stable conditions with damped, forced convection (Thom 1975). A stable atmosphere, with H directed toward the lake surface, was common for most of the ice-free period (i.e., until early September 1998; Blanken et al. 2000). Only in the late fall did the direction of H reverse, and an unstable atmosphere prevailed.

The power spectral density, $S_s(f)$, of the time series of s, and the cospectral or cross-spectral density of s and w, $C_{ws}(f)$, were estimated using Welch's averaged periodogram method (Math Works, Inc.). For both spectral densities, a fast Fourier transform length of 2^9 was used with nonoverlapping Hanning windows of the same length. One hour of the high-frequency data were used, thus, all time series consisted of 36 000 values, detrended by removing the mean. Both spectral densities were multiplied by f to enhance the higher frequencies, and $fS_s(f)$ and $fC_{ws}(f)$ were standardized by the variance of s and the absolute value of the covariance be-

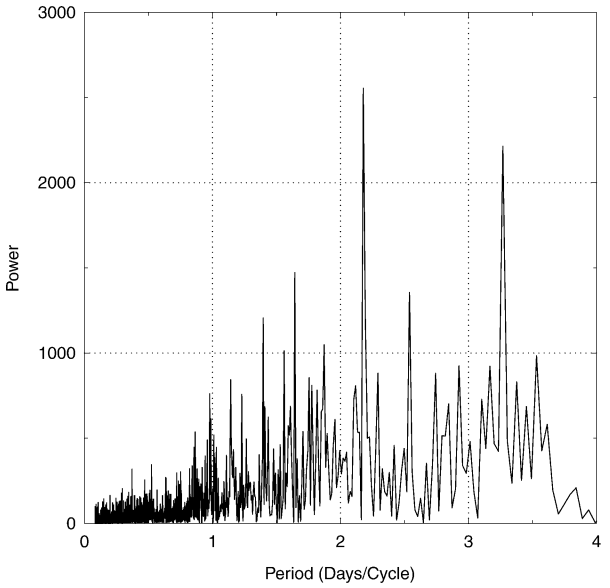

FIG. 3. Power spectra of the finite Fourier-transformed hourly evaporation. Data from all 3 yr are included. The prominent evaporation cycle was at 2.18 days, with secondary cycles at 3.27, 1.64, and 2.54 days.

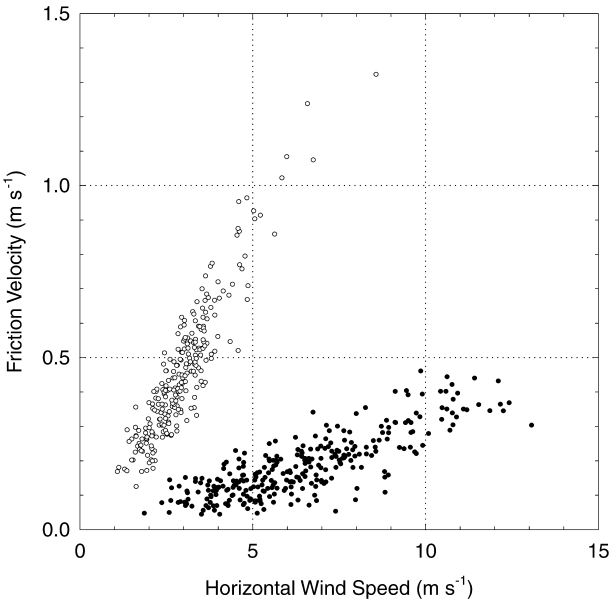

FIG. 4. Relationship between the daily mean friction velocity (u^*) and the horizontal wind speed (u) for a boreal aspen forest (open circles) (see Blanken et al. 2001) and Great Slave Lake (closed circles; data from all 3 yr). The ratio u^*/u is equivalent to the drag coefficient if u at the surface is 0.

tween w and s, respectively. For clarity, means within 50 equally spaced logarithmic intervals were plotted. Spectra were plotted against the nondimensional frequency $n = fz/\overline{u}$ (see Figs. 11 through 13).

Several other measurements were made at the site, including water surface or ''skin'' temperature (T_0), measured with an infrared thermometer (Everest Interscience, model 4000. GL) with a 15° field of view. An unobstructed view of the water surface was achieved by mounting the instrument at the end of a boom extending horizontally approximately 14 m beyond the shore, and 2 m above the water surface. Aimed at a 45° angle, this configuration resulted in a 4.6 m^2 viewing area (in 1999, the thermometer was relocated farther away from the water's edge). The infrared thermometer was specifically designed for marine applications, and its location far from the water's edge kept the instrument away from splash and spray. Meteorological measurements were taken independently of the Hydra from a separate 9-m-tall tower (approximately 18 m above the mean water surface). Measurements included wind speed and direction (R. M. Young, model 5310), and relative humidity (Vaisala, HMP-35D, and R. M. Young radiation shield model 41002). Dataloggers (Campbell Scientific, models models CR10X or 21X), scanning and averaging at 5-s and 15-min intervals, respectively, collected and stored data with power supplied by solar panel–charged 12-V batteries.

4. Results and discussion

Given the lake's large volume of water, and hence, thermal inertia, it is reasonable to predict a conservative seasonal pattern of evaporation and the surface energy balance with small interannual differences. Figure 2 reveals, however, that the daily variability was often sufficient to result in interannual variability. For example, the seasonal trend for λE was to increase with time peaking just before freeze up, yet superimposed on this trend was pronounced variation in the daily mean λE throughout the ice-free period (Fig. 2a). Any variability in H (Fig. 2b) was suppressed for much of the season, because H was small until late in the year when the air temperature decreased below the water surface temperature. The evaporative fraction, E_F, did reveal this large daily variability in λE, relative to the sum of λE plus $H[E_F = |\lambda E|/(|\lambda E| + |H|)]$. Not shown by the seasonal patterns in either λE or H alone, E_F peaked in approximately late August, after increasing through a period when the atmosphere was stable (Fig. 2c), due primarily to the warm air aloft of the cold water surface. The air temperature inversions and corresponding downward-directed H, and the low friction velocities resulted in a stable atmosphere (quantified by the measurement height, z, divided by the Monin–Obukhov length, L) for much of the ice-free periods (Fig. 2d). What then is the process responsible for these periodic ''pulses'' of evaporation that are sufficient to maximize the evaporative fraction at a time when the atmosphere suppresses turbulent exchange?

To begin examining this issue, first the duration of these evaporation pulses that appear in the seasonal pattern was quantified by using a finite Fourier transformation to convert the hourly time series of E to a fre-

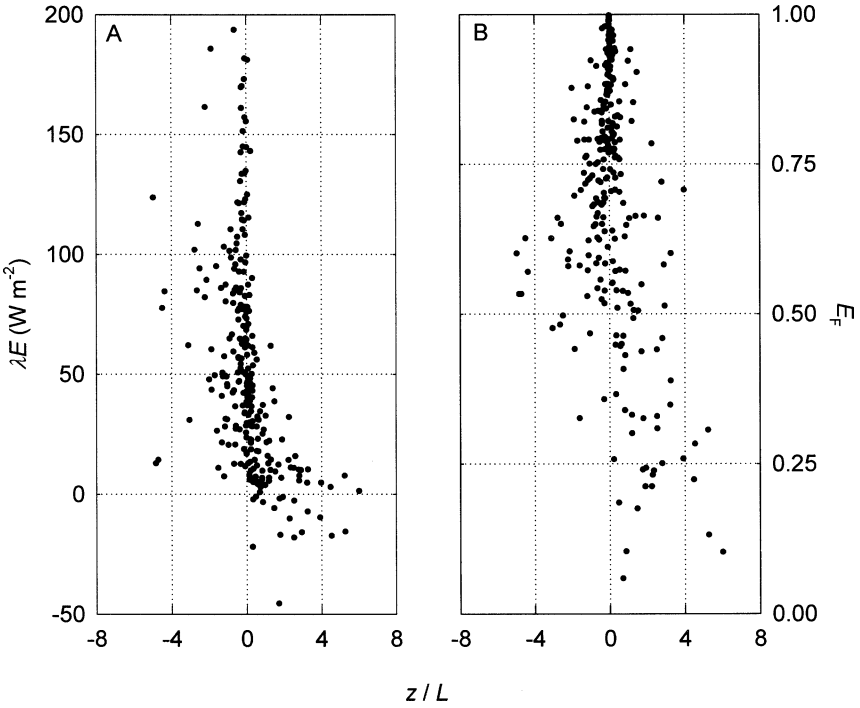

FIG. 5. Relationship between the 24-h (UTC) mean atmospheric stability, quantified by the measurement height divided by the Monin–Obukhov stability length (z/L) and the latent heat flux (A, λE), or the evaporative fraction (B, E_F). Data from all 3 yr are included.

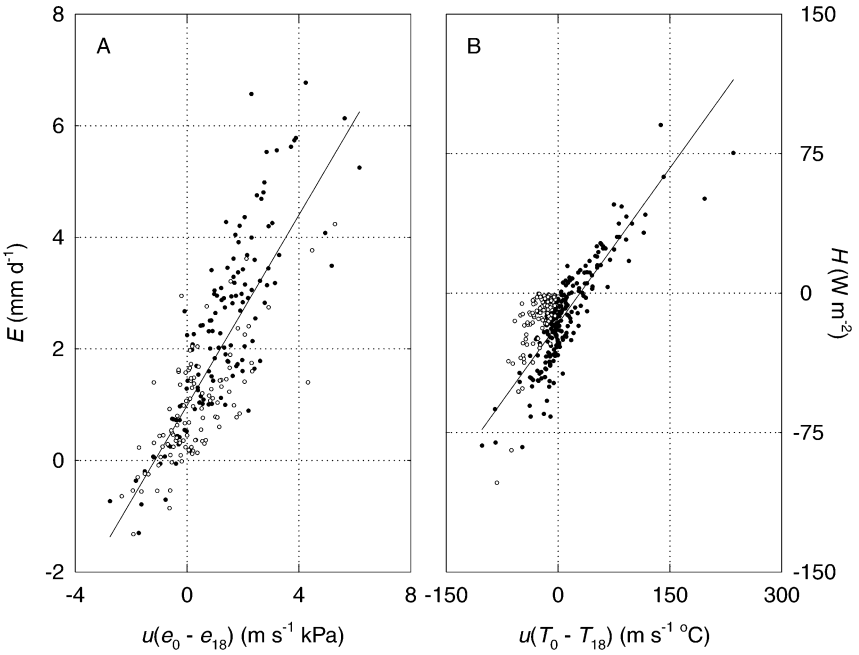

FIG. 6. Relationship between the 24-h (UTC) mean product of the horizontal wind speed and the difference in vapor pressure between the water surface and measurement height, and the daily total evaporative water loss (A), or the mean product of the horizontal wind speed and the difference in temperature between the water surface and measurement height, and the daily mean sensible heat flux (B). Days with a stable atmosphere ($z/L > 0.01$) are shown (open circles). Linear regressions are shown by the line, for (A), $y = 0.85x + 0.98$, $r^2 = 0.66$, and for (B), $y = 0.56x - 16.4$, $r^2 = 0.74$. Data from all 3 yr are included.

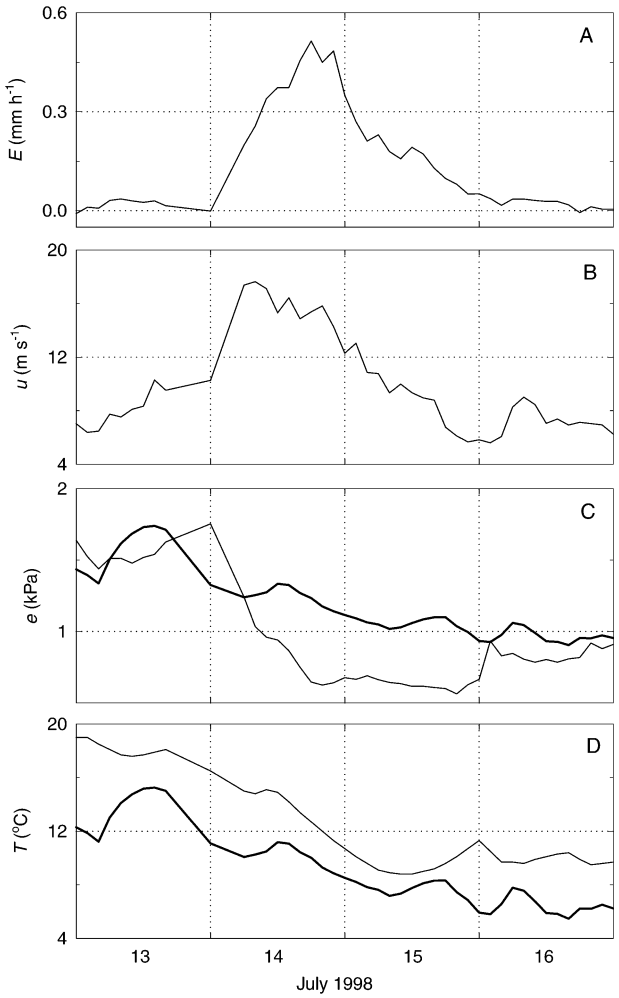

FIG. 7. Example of a relatively short evaporation pulse during stable atmospheric conditions in 1998. Evaporation (A) increased in response to an increase in the horizontal wind speed (B), and the vapor pressure in the atmosphere (thin line) decreased below that at the water surface (thick line) (C). During this period, air temperature (thin line) remained above water surface temperature (thick line) (D). Mean hourly data are plotted.

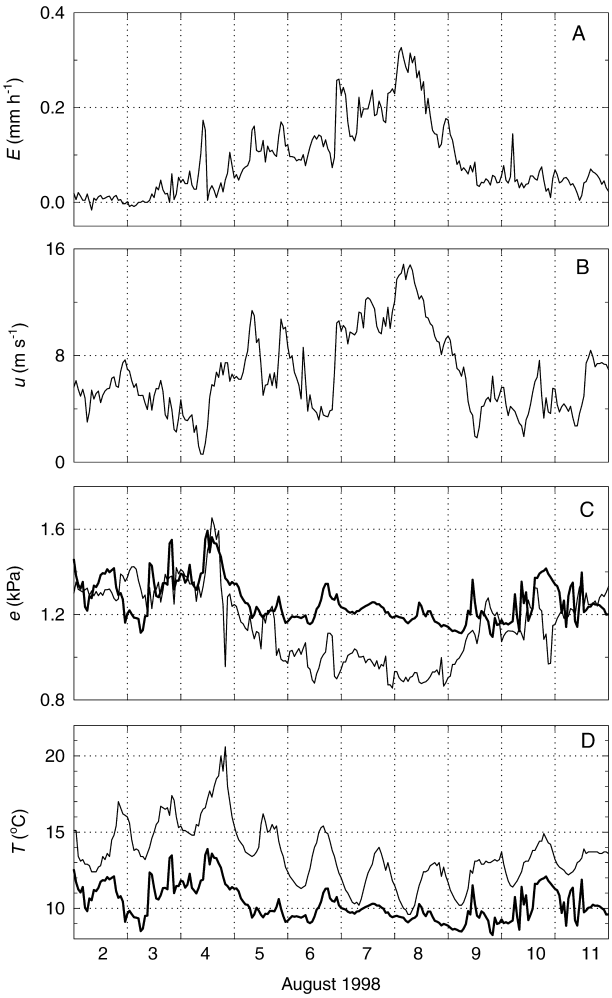

FIG. 8. Example of a relatively long evaporation pulse during stable atmospheric conditions in 1999. Again, evaporation (A) increased in response to an increase in the horizontal wind speed (B), and the vapor pressure in the atmosphere (thin line) decreased below that at the water surface (thick line) (C). During this period, air temperature (thin line) remained above the water surface temperature (thick line) (D). Mean hourly data are plotted.

quency scale, and then a power spectral density function to calculate the strength or power associated at each of the frequencies was applied (here shown as period, $1/f$). Figure 3 shows prominent, statistically significant peaks in the power spectra of the daily total E at 2.18 days (52 h), followed by another at 3.27 days (78 h), with secondary peaks at 2.54 (61 h) and 1.64 days (39 h). Therefore, an evaporation pulse is defined as occurring in Fig. 2a when the 24-h mean λE is at least twice the value of the 10-day running mean, and is considered to begin and end 1 day to either side of when the pulse occurred to encompass the prominent 52–78-h period, as indicated from Fig. 3. The contribution of these evaporation pulses (4, 12, and 14 pulses in 1997, 1998, and 1999, respectively), based on the total evaporation including 1 day before and after a pulse, were 45% (1997), 65% (1998), and 47% (1999) of the measured totals. Days with pulses, however, constituted only 24% (1997), 37% (1998), and 25% (1999) of the total number of days observed. Their role was especially significant in 1998, when the mean annual air temperature in Yellowknife was 4°C above the 1961–90 mean (Blanken et al. 2000).

During a large portion of the ice-free season, when the air heats faster and warms much more than the lake, convectively driven turbulence above the lake is suppressed. Mechanically driven turbulence (forced convection) could be effective in increasing turbulent exchange during these periods over terrestrial surfaces, but is inefficient over water surfaces, which can deform under wind stress. For example, Fig. 4 contrasts the relationship between friction velocity and horizontal wind speed for both a forest (boreal aspen; see, Blanken

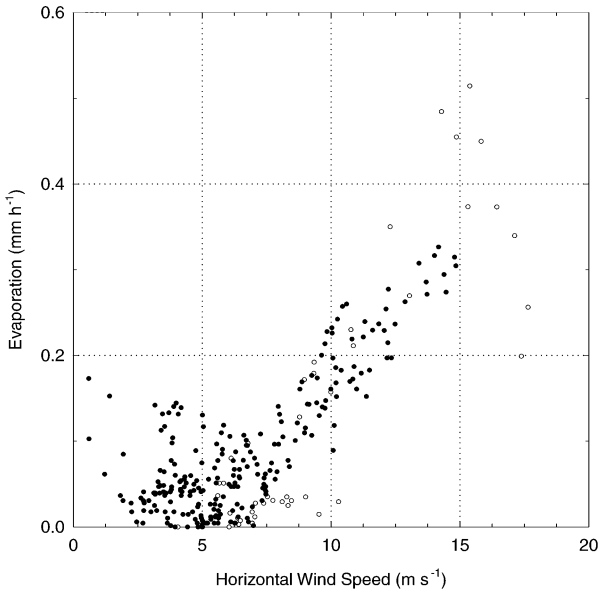

FIG. 9. Relationship between hourly evaporation and the horizontal wind speed during the evaporation events shown in Fig. 7 (1998, open circles) and in Fig. 8 (1999, closed circles). Evaporation increased only after horizontal wind speeds exceeded approximately 8 m s^{-1}.

et al. 2001 for details) and the lake (the slope of this relationship is equivalent to the drag coefficient if u at the surface is 0). The lake is much less effective than the forest at generating friction at a given u. Figure 5a shows that λE decreased substantially as atmospheric stability increased, yet the relationship between λE and atmospheric stability became poorly defined and had its greatest variability as z/L approached 0. The same was true for E_F (Figure 5b). Because z/L approaches 0 as the friction velocity (u^*) increases and H approaches 0, near-neutral atmospheric stability conditions are often indicative of windy conditions. Calm conditions interrupted by intermittent gusts could also result in the calculation of a small H and large u^*, hence, a near-zero z/L. This may explain the large variability in λE and E_F in near-neutral stability conditions, because either persistently strong or intermittently gusty winds could both give a near-zero z/L when averaged over a typical 30- or 60-min period.

Figure 6a shows that, regardless of the state of atmospheric stability, the daily total E increased roughly linearly as function of the product u and the difference between the saturation vapor pressure, calculated at water surface temperature, $e^*(T_0) = e_0$, and the atmospheric vapor pressure, $e_a(\Delta e = e_0 - e_a)$. Similarly, the daily mean H was correlated with the product of u and the difference between water surface and air temperature (Fig. 6b). As expected, stable periods coincide with air temperature inversions (H negative and directed toward the surface).

Figure 6 essentially confirms what is well known about the controls of evaporation from a well-watered surface with no surface resistance to vapor transfer (excluding the laminar boundary layer resistance), which forms the concept of ''potential'' evaporation. This states that if there is energy available, at the expense of

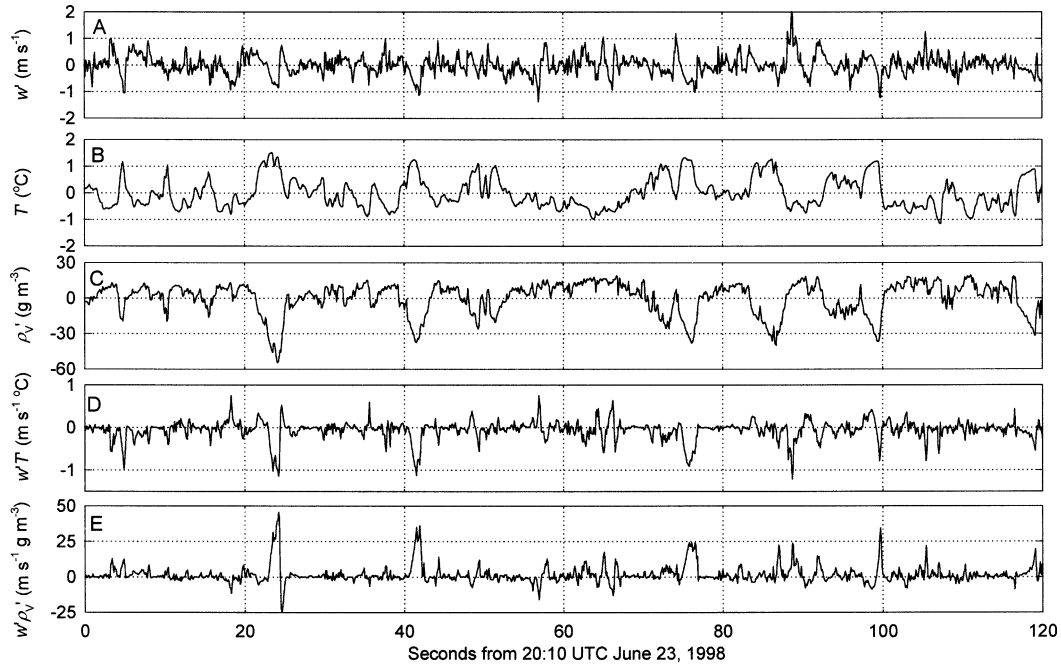

FIG. 10. Sample 2-min time series of linearly detrended vertical wind speed (A, w'), air temperature (B, T'), vapor density (C, ρ_v'), and the product of $w'T'$ (D) and $w'\rho_v'$(E). Note the bursts in E corresponding to downdrafts of warm, dry air. Data were sampled at 10 Hz, beginning at 2010 UTC 23 Jun 1998.

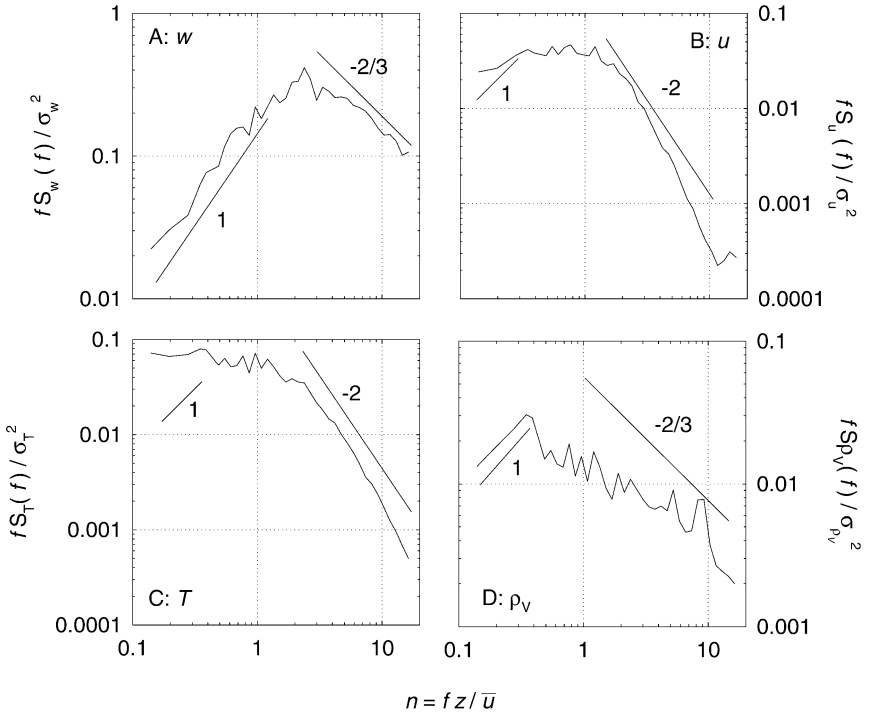

FIG. 11. Power spectrum for the vertical (A, w) and horizontal (B, u) wind velocity components, and the air temperature (C, T) and vapor density (D, ρ_v) scalars. Each were multiplied by the frequency (f) and standardized by their respective variance (σ^2). Spectral densities were plotted against the nondimensional frequency $n = fz/\overline{u}$. Straight lines represent the indicated slopes.

heat, this energy can be used for evaporation at a rate proportional to the water vapor gradient, which itself is influenced by the wind insomuch as the advection of dry air can decrease e_a, and, hence, increase Δe. What is the source of this dry air above the lake, and how does it reach the lake surface? Given the sheer size of the lake, and the large distance between the measurement site and shore, measurements were not in the transition zone where the air blowing onto the lake adjusts to its new surface (in fact, onshore winds were likely during the stable period). Yet, given the small H from the lake for most of the season, the convective boundary layer depth above the lake will be shallow (ca., $<$50 m), relative to the depth of the convective boundary layer above the surrounding rocky, barren Canadian Shield terrain where H would be large. This would, then, result in a strong horizontal barometric pressure gradient across the lake, with strong winds blowing onshore. It is proposed that the air above the lake must then be replaced by descending adiabatically warmed air from the surrounding terrain. Thus, under passive synoptic conditions, such mesoscale lake-induced circulation would develop, constantly resupplying the lake with a source of relatively warm, dry air. This circulation could be interrupted with the passage of frontal systems, or be reversed late in the ice-free period, when horizontal barometric pressure gradient reverses (offshore flow).

Therefore, a working hypothesis is that this warm, dry air situated in an inversion layer above the lake enhances evaporation when mixed down to the lake surface below. This represents a transition in spatial and temporal scales from long-term, large-scale lake breeze circulation (hours, tens of kilometers) to the short-term, small-scale turbulent interjection (seconds, meters) of warm, dry air across the temperature inversion. The entrainment of this air should explain the observed evaporation pulses. In the results and discussion that follows, evidence for and quantification of this vertical entrainment is presented.

Two examples, one in 1998 (Fig. 7) and one in 1999 (Fig. 8) illustrate the enhancement of E over the dominant spectral periods shown in Fig. 3. In both figures, despite the atmosphere being stable at all times (Figs. 7d and 8d show that temperature inversions persisted), E increased with u. The hypothesis is that the subsequent decrease in e_a below e_0 (hence, the large increase in E) was a result of the intermittent injection or pumping of warm, dry air from above. Figure 9 illustrates that for the two periods shown in Figs. 7 and 8, E increased linearly with u after a threshold of approximately 8 m s^{-1} was reached. This is near the 10 m s^{-1} u threshold where the evaporation of sea spray can contribute roughly 10% of the total λE (Andreas and Decosmo 2002). Horizontal convective rolls can form at any wind speed (Weckwerth et al. 1999), but if they did form (no cloud streets were observed neither visually at the site nor

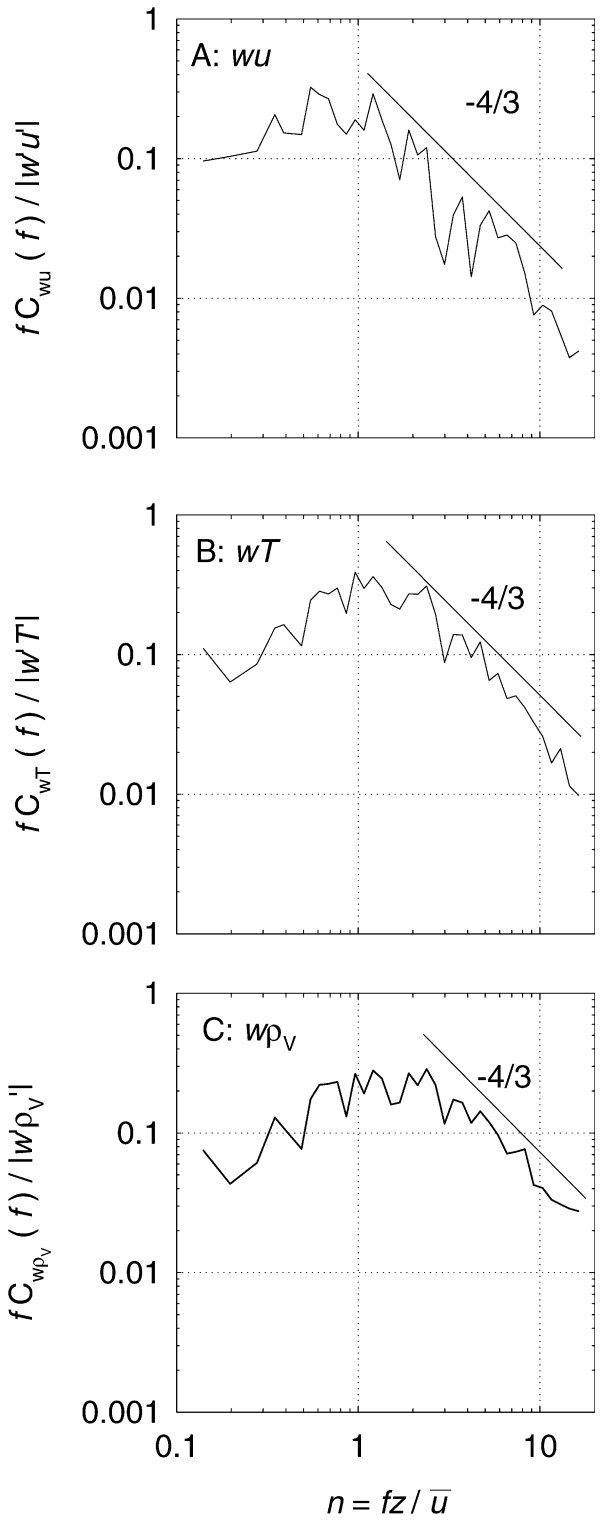

FIG. 12. Cospectrum for the vertical (w) and horizontal wind velocity components (A, wu), air temperature (B, wT), and vapor density (C, $w\rho_v$). Each were multiplied by the frequency (f) and standardized by the absolute value of their respective covariances. Cospectral densities were plotted against the nondimensional frequency $n = fz/\overline{u}$. Straight lines represent the indicated slopes.

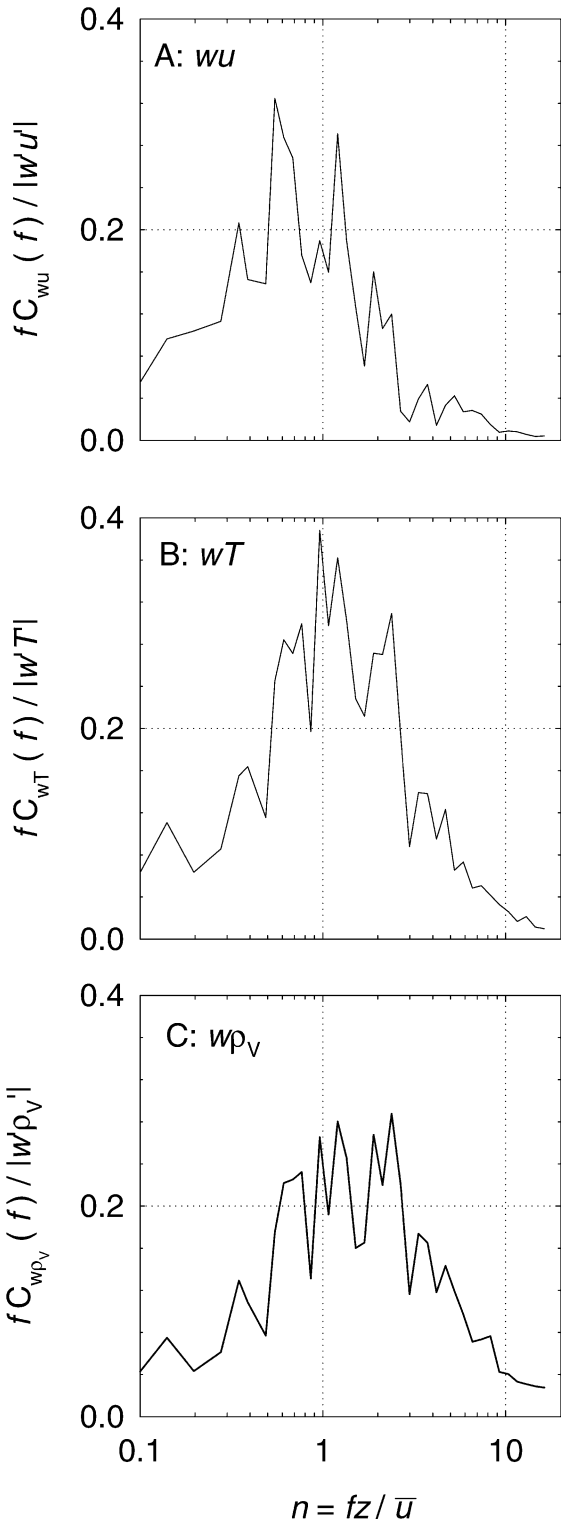

FIG. 13. Same as Fig. 12, except plotted using semilog axes.

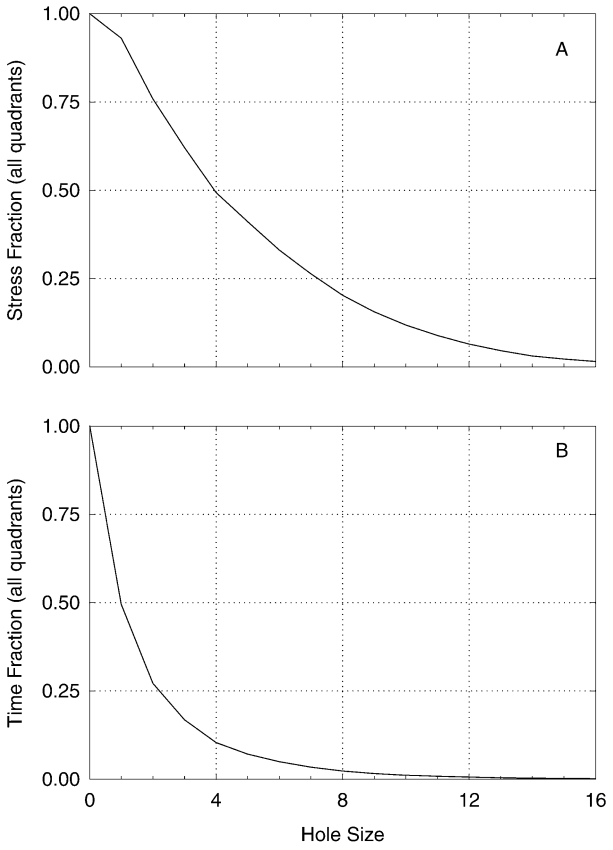

FIG. 14. Sum of the stress (A) and time fractions (B) for the four quadrants at varying hole sizes for the period described in Table 1.

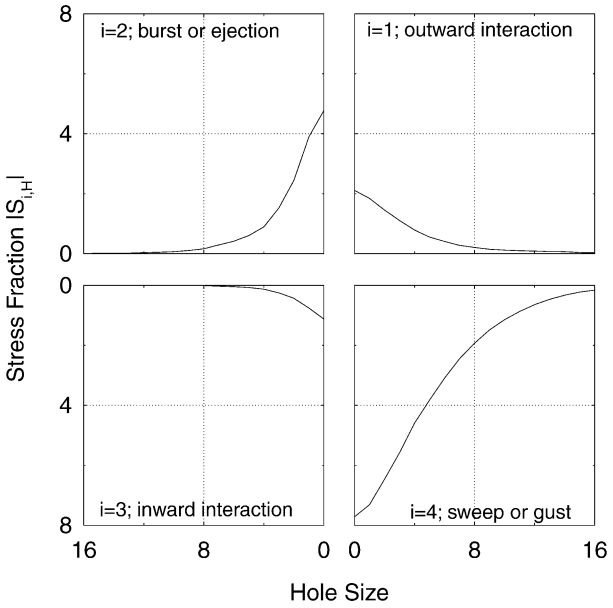

FIG. 15. Stress fractions for each of the four quadrants during the period described in Table 1.

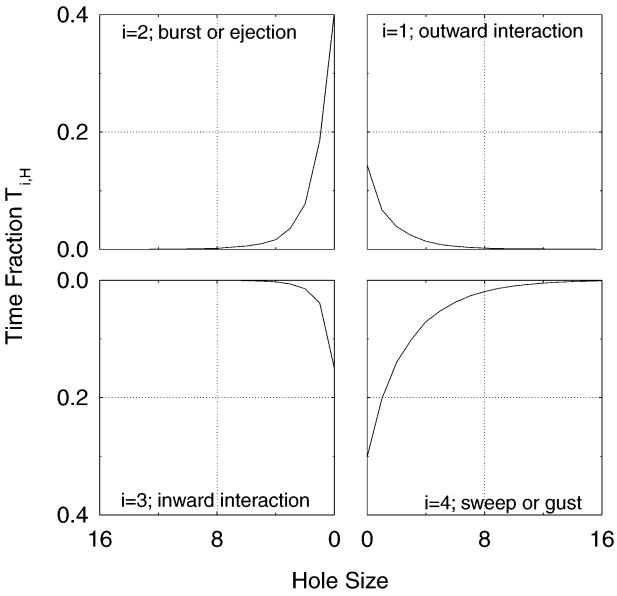

FIG. 16. Time fractions for each of the four quadrants during the period described in Table 1.

from satellite images), they likely only enhanced λE by less than 10% (Renfrew and Moore 1999). Perhaps in this case, weakly developed convective rolls, wind shear, or gravity waves along the air temperature inversion were sufficient to generate persistent downdrafts of the warmer, drier air through the shallow convective boundary layer.

The exact nature of this injection or pumping of warm, dry air from above, and its effects on λE and H, is illustrated in the time series of high-frequency data collected during a period when the atmosphere was stable (Fig. 10; see Table 1 for a statistical summary of the frequency distributions of w, u, T, and ρ_v). The descending air was markedly warm and dry. The high covariance between w and T resulted in a large negative H during these downdrafts, and, similarity, the high covariance between w and ρ_v during these downdrafts resulted in large evaporation. Over the 2-min period shown in Fig. 10, several of these injection events occurred, and, when aggregated over 60 min, resulted in a large E that otherwise may have been missed if only mean values were used to calculate E using, for example, the mass transfer technique.

TABLE 1. Statistics (scalar mean $\overline{s}$, standard deviation σ, skewness Sk, and kurtosis Kr) describing the frequency distributions of the vertical speed w, horizontal wind speed u, air temperature T, and vapor density ρ_v collected at 10 Hz for 1 h beginning 2010 UTC 23 Jun 1998.

	w	u	T	ρ_v
$\overline{s}$	0.71 m s^{-1}	5.19 m s^{-1}	7.91°C	6.58 g m^{-3}
σ	0.30 m s^{-1}	0.73 m s^{-1}	0.51°C	15.76 g m^{-3}
Sk	−0.24	0.24	0.86	−0.24
Kr	5.00	2.00	4.11	5.00

At this point, note the fractal behavior of the ratio of the evaporative flux fraction to time fraction relative to the aggregation time. When the evaporation pulse was defined as occurring at a timescale of days (see Fig. 2), the ratio of evaporation that occurred during these times was almost twice the fraction of time that they occupied; these ratios were 1.85, 1.76, and 1.88, for 1997–1998, respectively. At a finer timescale of 10 Hz, however, this ratio was 8.75 (from Fig. 10, 70% of the evaporation occurred during the fast pulses lasting only 8% of the time), indicating the evaporation pulses represented substantially more of the total evaporation. A similar behavior was also observed for the momentum flux (see Fig. 14).

To determine both the quality of the measurements during these periods, and gain information on the physical structure of these downward-directed eddies, the power spectrums for w, T, ρ_v, and u were plotted (Fig. 11). The spectra of a time series shows the energy contained at individual frequencies, after the time series consisting of one variable has been converted to a frequency scale using a finite Fourier transformation. In general, the range of frequencies where energy is being produced (energy production range) can be identified by the rising limb of the spectra, with an expected slope of 1. The spectral peak indicates the frequency where most of the energy is contained, and the falling limb represents the range of frequencies where energy is neither produced nor dissipated, but is transported by progressively smaller scales. The expected slope in this so-called inertial subrange is $-2/3$ when plotted on a log–log scale (Kaimal and Finnigan 1994). This technique has been used to examine the structure of turbulence over oceans (e.g., Miyake et al. 1970; Pond et al. 1971) and large lakes (e.g., Smith 1974; Drennan et al. 1999).

The w spectrum (Fig. 11a) showed an energy production range with a slope of 1 roughly between $0.1 < n < 1.0$. The inertial subrange, roughly between $1.0 < n < 10.5$, exhibited the expected $-2/3$ slope. The u spectrum (Fig. 11b) showed an energy production range with a slope <1, rather than the theoretically predicted slope of 1, over a range of roughly $0.1 < n < 1.0$. This indicated u energy was not being produced as quickly as expected, perhaps because shear-generated energy production was weak over the aerodynamically smooth lake surface. The inertial subrange showed a slope closer to -2 between $1.0 < n < 10.0$, steeper than the expected $-2/3$ slope. This indicated that energy was cascading to smaller scales faster than expected, but this was likely an artifact of slow sensor response, especially towards the higher frequencies (frequency response corrections were applied to all flux calculations, and were typically of the order of two for the momentum flux; Shuttleworth et al. 1988). The inflection at $n \approx 10$ was likely white noise in the sensor, but the wu cospectrum (Fig. 12a) showed that the contribution of this noise to flux measurements at this high frequency was small.

The energy production ranges for the scalars T (Fig. 11c) and ρ_v (Fig. 11d) were small. Similar to the u spectrum, the inertial subrange slope for the T spectrum was closer to -2 than the expected $-2/3$, which was more closely followed by the ρ_v spectrum. Again, this was likely an artifact of slow sensor response. The spectral peak for T occurred at $n = 0.37$, with a secondary peak at $n = 1.02$ before falling into the inertial subrange. These corresponding to a λ_T of 17.6 m and 48.6 m, $n = 1.02$ and 0.37, respectively. The spectral peak for ρ_v occurred at $n = 0.28$, corresponding to $\lambda_v = 64.3$ m. The spectral peaks for both T and ρ_v occurred at a much larger λ than that for w and u, indicating that scalar transport was dominant during the energy production stage of w and u.

When plotted on a log–log scale, the cospectra for wu, wT, and $w\rho_v$ (Figs. 12a, 12b, and 12c, respectively) all show the expected slope of $-4/3$ (Wyngaard and Coté 1972, Kaimal and Finnigan 1994) in the inertial subrange. The cospectral peaks, indicating the beginning of the inertial subrange, for wT and $w\rho_v$ were shifted toward higher frequencies by $n \approx 0.6$, indicating that heat and water vapor were transported more effectively by the smaller eddies, and momentum by the larger, lower-frequency eddies.

Plotting cospectra using semilog axes has the advantage of maintaining an area proportional to the covariance between w and s, thus, allowing a direct indication of the contribution from eddies at various frequencies (ca., size) to the flux (Fig. 13). The contributions from eddies to wu decreased at $n > \approx 2$ ($f = 0.6$ Hz) (Fig. 13a), yet were still substantial for wT (Fig. 13b) and $w\rho_v$ (Fig. 13c). The wu and wT cospectra approached zero by $n \approx 20$ ($f = 5.8$ Hz), yet were still greater than zero for $w\rho_v$. This indicates that the sampling frequency was adequate for capturing any high-frequency u and T contributions to their respective fluxes (this shows that the slow u sensor response did not result in an underestimation of the momentum flux), but a faster ρ_v response was required, although the contribution at these high frequencies was minimal.

These spectral and cospectral analyses has given insight into the structure of the downdrafts that are responsible for most of the water vapor, heat, and momentum transfer during periods of atmospheric stability. One final analysis was used to further document these intrusions of warm, dry air from above. Here, a conditional sampling technique (quandrant-hole analysis) was employed to describe in detail the structure of the tangential momentum stress, or the kinds of turbulent motion that dominate momentum transfer, and thus, likely also the transfer of water vapor and heat (e.g., Finnigan 1979; Baldocchi and Hutchinson 1987).

This technique determined the contribution of the instantaneous product of w' and u' to the calculation of the mean covariance $\overline{w'u'}$. The ratio $|w'u'|/|\overline{w'u'}|$ is known as the hole size, H. The four quadrants were defined as follows: outward interaction ($i = 1$; $u' > 0$, i.e., the anomaly in the horizontal wind vector is such

that its scalar magnitude is increased, $w' > 0$), burst or ejection ($i = 2$; $u' < 0$, $w' > 0$), inward interactions ($i = 3$; $u' < 0$, $w' < 0$), and sweep or gust ($i = 4$; $u' > 0$, $w' < 0$). A stress fraction is defined as

$$S_{i,H} = \frac{1}{|\overline{u'w'}|}\frac{1}{L}\int_0^L w'(t)u'(t)I_{i,H}\,dt, \tag{2}$$

and the time fraction associated with the turbulent events is defined as

$$T_{i,H} = \frac{1}{L}\int_0^L I_{i,H}(t)\,dt, \tag{3}$$

where $I_{i,H}$ equals 1 if $\underline{u'}$ and w' lie on the ith quadrant and $|w'u'| >= H|\overline{w'u'}|$, and equals 0 otherwise, L is the length of the averaging period, and t is time.

Above the lake, the intermittent nature of momentum transfer during this stable period is revealed in Fig. 14. Half of the total stress fraction resulted from events with a hole size greater than approximately 4 (Fig. 14a), and these events occurred only 11% of the time (Fig. 14b). This means that half of the momentum was transferred intermittently, when the instantaneous product of w' and $\underline{u'}$ was 4 times greater than the mean covariance, $\overline{w'u'}$. This result is further evidence of the intermittent nature of turbulent transfer during the period of atmospheric stability.

Figure 15 shows the stress fractions in each quadrant as a function of hole size. Sweeps or gusts clearly provided the main mechanism for momentum transfer, followed by bursts or ejections. The relative importance of sweeps relative to the other kinds of turbulent transfer can be determined by examining the ratios of stress fractions when the hole size is zero. The ratios of the stress fractions of sweeps to bursts or ejections, outward interactions, and inward interactions, were 1.62, 3.67, and 6.85, respectively. This shows that these downward-directed gusty sweeps and subsequent ejections from the surface were the dominant turbulent transfer mechanism.

The largest time fractions were associated with sweeps and bursts, with much smaller and nearly equal time fractions spent of outward and inward interactions (Fig. 16). At a hole size of zero, the ratios of the time fractions for bursts or ejections to sweeps, inward ejections, and outward ejections were 1.35, 2.69, and 2.82, respectively. Thus, although the time fraction for sweeps and bursts at a hole size of zero was slightly less than that for bursts or ejections, it was larger at most other hole sizes, indicating the importance of these events.

5. Conclusions

This study has highlighted the contribution and role of short-term evaporation events in the total seasonal evaporation, events that appear as ''pulses'' of evaporation superimposed on the background, long-term trend in the seasonal evaporation rates. During three seasons of measurements, these events contributed between 45%–65% of the total measured evaporation, yet lasted only 24%–37% of the observation periods, thus, any perturbations in the mechanisms that affect this entrainment will affect the annual evaporative water loss just as significantly as the ice formation and breakup dates. These evaporation events were identified to be the result of the entrainment of warm, dry air in the atmosphere down to the lake surface. During 1998, when air temperatures were above average, the vigor of these events, as expected, increased and accounted for 65% of the total measured evaporation. Therefore, the presence of warmer, drier air above the lake at any time when the lake is ice free will increase evaporation through the mechanism described here. In the late fall and early winter, this effect is exacerbated, because the entrainment of warm, dry air not only enhances evaporation, but also helps to maintain ice-free conditions by this intermittent pumping of warm air to the lake surface. The strength of this positive feedback between entrainment and prolonging ice-free condition was demonstrated in 1998, and will likely occur again when similar conditions prevail.

This study confirms that the background, long-term seasonal trend in the evaporation rate, as in the southern Laurentian Great Lakes, steadily increased as the ice-free season progressed. Maximum evaporation rates are achieved just before the lake freezes when the lake-to-air vapor pressure gradient is at its maximum. Thus, a later freeze-up date may result in significantly more evaporative water loss than an earlier breakup date. These dates, however, are not mutually exclusive. An earlier breakup date may permit more heat, in the form of absorbed solar radiation, to be stored in the lake and, subsequently, be released later in the year, thereby delaying the freeze-up date. This behavior is completely different from terrestrial surfaces. Evaporation from these surfaces tends to be controlled by energy availability, thus, the evaporation rate peaks near the summer solstice. Throughout the Mackenzie basin, dotted with its many small, shallow lakes and wetlands, the evaporation rate would, therefore, be a strong function of the available energy, with maximum evaporation rates, on average, attained around the summer solstice at the end of June. Great Slave and Great Bear Lakes, however, provide a strong source of water vapor to the atmosphere late in the year at a time when the terrestrial surface does not, thus, altering the water balance of the Mackenzie basin.

This paper has shown that lake evaporation does not passively occur as a function of long-term, large-scale differences between lake and atmospheric conditions, such as temperature, humidity, and wind. Rather, the processes affecting evaporation at these scales are an aggregate of short-term, small-scale turbulence, perhaps linked by fractal behavior. Understanding the integration of the processes across these temporal and spatial scales allows for a better understanding of the sensitivity of

the lake to climate change, and, therefore, improvement of the ability to model the potential effects of climate change at high latitudes where lakes are an important part of the ecosystem.

As this paper began with a hypothesis, and so too will it end: The annual evaporative water loss from large, northern lakes will increase nonlinearly with increasing air temperatures, due to the entrainment process and associated positive feedback with ice conditions described herein.

Acknowledgments. The collective efforts of many made this study possible, and we apologize to those who unintentionally were not specifically mentioned. From the Yellowknife branch of Environment Canada, Chris Spence and Jesse Jasper assisted with logistics. The Royal Canadian Mounted Police Marine Unit, based in Yellowknife, provided safe and courteous transportation to the study site. The Yellowknife branch of the Water Survey of Canada generously loaned equipment and courteously provided warehouse space in Yellowknife. Dale Boudreau, Alistair Culf, Mike Stroud, and Cliff Brettle gave invaluable technical assistance. Reviews of this manuscript by Dr. Dean Anderson of the U.S. Geological Survey, and the anonymous journal reviewers and editorial staff were greatly appreciated, as were comments provided by Geoff Strong, Kit Szeto, Peter Yau, and others at the CAGES workshop. This research would not be possible without family support and understanding both in and out of the field.

REFERENCES

Andreas, E. L, and J. Decosmo, 2002: The signature of sea spray in the HEXOS turbulent heat flux data. *Bound.-Layer Meteor.,* **103,** 303–333.

Baldocchi, D. D., and B. A. Hutchinson, 1987: Turbulence in an almond orchard: Vertical variations in turbulent statistics. *Bound.-Layer Meteor.,* **20,** 127–146.

Bates, N. R., and L. Merlivat, 2001: The influence of short-term wind variability on air–sea CO_2 exchange. *Geophys. Res. Lett.,* **28,** 3281–3284.

Blanken, P. D., and Coauthors, 2000: Eddy covariance measurements of evaporation from Great Slave Lake, Northwest Territories, Canada. *Water Resour. Res.,* **36,** 1069–1077.

——, T. A. Black, H. H. Neumann, G. den Hartog, P. C. Yang, Z. Nesic, and X. Lee, 2001: The seasonal water and energy exchange above and within a boreal aspen forest. *J. Hydrol.,* **245,** 118–136.

Drennan, W. M., K. K. Kahma, and M. A. Donelan, 1999: On momentum and velocity spectra over waves. *Bound.-Layer Meteor.,* **92,** 489–515.

Finnigan, J. J., 1979: Turbulence in waving wheat. II: Structure of momentum transfer. *Bound.-Layer Meteor.,* **16,** 213–236.

Heikinheimo, M., M. Kangas, T. Tourula, A. Venäläinen, and S. Tattari, 1999: Momentum and heat fluxes over lakes Tämnaren and Råksjö determined by the bulk-aerodynamic and eddy-correlation methods. *Agric. For. Meteor.,* **98–99,** 521–534.

Hudson, E., 1991: *Marine Guide to Local Conditions and Forecasts: Great Slave Lake, Lake Athabasca, Lake Winnipeg, Lake of the Woods, Lake Nipigon.* Ministry of Supply and Services, 130 pp.

Kaimal, J. C., and J. J. Finnigan, 1994: *Atmospheric Boundary Layer Flows: Their Structure and Measurement.* Oxford University Press, 289 pp.

Laird, N. G., and D. A. R. Kristovich, 2002: Variations of sensible and latent heat fluxes from a Great Lakes buoy and associated synoptic weather patterns. *J. Hydrometeor.,* **3,** 3–12.

Miyake, M., M. Donelan, G. McBean, C. Paulson, F. Badgely, and E. Leavitt, 1970: Comparison of turbulent fluxes over water determined by profile and eddy correlation techniques. *Quart. J. Roy. Meteor. Soc.,* **96,** 132–137.

Pond, S., G. T. Phelps, and J. E. Paquin, 1971: Measurements of the turbulent fluxes of momentum, moisture and sensible heat over the ocean. *J. Atmos. Sci.,* **28,** 901–917.

Rawson, D. S., 1950: The physical limnology of Great Slave Lake. *J. Fish. Res. Can.,* **8,** 3–66.

Renfrew, I. A., and G. W. K. Moore, 1999: An extreme cold-air outbreak over the Labrador Sea: Roll vortices and air–sea interactions. *Mon. Wea. Rev.,* **127,** 2379–2394.

Rouse, W. R., and Coauthors, 2003a: Energy and water cycles in a high-latitude north-flowing river system. *Bull. Amer. Meteor. Soc.,* **84,** 73–87.

——, C. M. Oswald, J. Binyamin, P. D. Blanken, W. M. Schertzer, and C. Spence, 2003b: Interannual and seasonal variability of the surface energy balance and temperature of central Great Slave Lake. *J. Hydrometeor.,* **4,** 720–730.

Russell, L. M., D. H. Leschow, K. K. Laursen, P. B. Krummel, S. T. Siems, A. R. Bandy, D. C. Thornton, and T. S. Bates, 1998: Bidirectional mixing in an ACE 1 marine boundary layer overlain by a second turbulent layer. *J. Geophys. Res.,* **103,** 16 411–16 432.

Schertzer, W. M., W. R. Rouse, and P. D. Blanken, 2000: Cross-lake variation of physical limnological and climatological processes of Great Slave Lake. *Phys. Geogr.,* **21,** 385–406.

——, ——, ——, and A. E. Walker, 2003: Over-lake meteorology and estimated bulk heat exchange of Great Slave Lake in 1998 and 1999. *J. Hydrometeor.,* **4,** 649–659.

Schuepp, P. H., M. Y. Leclerc, J. I. MacPherson, and R. L. Desjardins, 1990: Footprint prediction of scalar fluxes from analytical solutions of the diffusion equations. *Bound.-Layer Meteor.,* **50,** 355–373.

Shuttleworth, W. J., J. H. C. Gash, C. R. Lloyd, D. D. McNeil, C. J. Moore, and J. S. Wallace, 1988: An integrated micrometeorological system for evaporation measurement. *Agric. For. Meteor.,* **43,** 295–317.

Smith, S. D., 1974: Eddy flux measurements over Lake Ontario. *Bound.-Layer Meteor.,* **6,** 235–255.

Stewart, R. E., and Coauthors, 1998: The Mackenzie GEWEX Study: The water and energy cycles of a major North American river basin. *Bull. Amer. Meteor. Soc.,* **79,** 2665–2683.

Sun, J. L., and Coauthors, 2002: Intermittent turbulence associated with a density current passage in the stable boundary layer. *Bound.-Layer Meteor.,* **105,** 199–219.

Thom, A. S., 1975: Momentum, mass and heat exchange of plant communities. *Principles,* J. L. Monteith, Ed., Vol. 1, *Vegetation and the Atmosphere,* Academic Press, 57–109.

Walker, A., A. Silis, J. Metcalf, M. Davey, R. Brown, and B. Goodison, 1999: Snow cover and lake ice determination in the MAGS region using passive microwave satellite and conventional data. *Proc. Fourth Scientific Workshop for the Mackenzie GEWEX Study (MAGS),* Montreal, QC, Canada, NSERC and AES, Environment Canada, 89–91.

Weckwerth, T. M., T. W. Horst, and J. W. Wilson, 1999: An observational study of the evolution of horizontal convective rolls. *Mon. Wea. Rev.,* **127,** 2160–2179.

Wyngaard, J. C., and O. R. Coté, 1972: Cospectral similarity in the atmospheric surface layer. *Quart. J. Roy. Meteor. Soc.,* **98,** 590–603.